THE JOURNAL OF PHYSICAL CHEMISTRY C

Article

pubs.acs.org/JPCC

How to Chemically Tailor Metal-Porphyrin-Like Active Sites on Carbon Nanotubes and Graphene for Minimal Overpotential in the Electrochemical Oxygen Evolution and Oxygen Reduction Reactions

Mu-Jeng Cheng,[†,‡] Martin Head-Gordon,*[,†,§] and Alexis T. Bell*[,†,‡]

[†]The Joint Center for Artificial Photosynthesis, Lawrence Berkeley National Laboratory, Berkeley, California 94720, United States

[‡]Department of Chemical and Biomolecular Engineering, University of California at Berkeley, Berkeley, California 94720, United States

[§]Department of Chemistry, University of California at Berkeley, Berkeley, California 94720, United States

Supporting Information

ABSTRACT: Density functional theory calculations are used to study the energetics of the electrochemical oxygen evolution reaction (OER) of water and the reverse oxygen reduction reaction (ORR) on metal-porphyrin-like centers incorporated into graphene layers or single-walled carbon nanotubes (SWCNTs). The objective is to explore the reductions in computational thermodynamic overpotential that can be achieved relative to catalysis on metal oxide surfaces (OER) or platinum (ORR) by varying the metal center and axial ligand. This permits a degree of simultaneous control over the free energy gap between the lowest energy OH and highest energy OOH intermediates, and the position of the oxo (O) intermediate in this gap. Optimal choice of metal toward the right of the first transition series largely controls the gap. Given a suitable metal such as Fe, the overpotential for OER can be tuned over a range greater than 0.35 V by choice of the axial ligand. For OER occurring within the SWCNTs, a minimum predicted overpotential of 0.35 V is found, very close to the gap-imposed limit of 0.30 V for this system. Similarly, the overpotential of ORR can be tuned over a range more than 0.30 V by selection of the axial ligand. While the calculations necessarily have limited accuracy, the principles should provide a transferable path toward overpotential optimization for the OER and ORR.

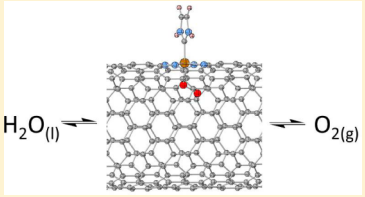

1. INTRODUCTION

Electrochemical water splitting holds considerable potential as a process for the production of carbon-free hydrogen using renewable sources of electrical power, such as wind and solar energy.[1,2] The splitting of water involves two half reactions: (a) the oxygen evolution reaction (OER), corresponding to water oxidation, $H_2O_{(l)} \rightarrow {}^1/_2O_2(g) + 2H^+ + 2e^-$, for which $E = 1.23$ V vs SHE at pH = 0, and (b) the hydrogen evolution reaction (HER), corresponding to proton reduction, $2H^+ + 2e^- \rightarrow H_2(g)$, for which $E = 0.00$ V vs SHE at pH = 0.

The efficiency of electrochemical water splitting is currently limited by substantial energy losses associated with high overpotentials for oxygen evolution (η^{OER}) at the anode. Even with the best heterogeneous catalysts, such as Ru oxides or Ir oxides, η^{OER} is typically greater than 0.30 V at a current density of 10 mA·cm^{-2}.[3] As a result, developing a strategy to minimize η^{OER} for existing classes of OER catalysts or discovering new catalyst types is an important objective for increasing the energy efficiency of electrochemical water splitting.

Correspondingly, when hydrogen is oxidized to water in a proton-exchange membrane fuel cells (PEMFC),[4,5] the oxygen reduction reaction (ORR), the reverse of OER, limits the fuel-cell efficiency. Currently, platinum is used as the main component of ORR catalyst for PEMFCs. It is also notable that even state-of-the-art systems operate at voltages of only ~0.7 V,[6] far below the equilibrium potential of 1.23 V. The high cost of platinum and the high ORR overpotential (η^{ORR}) constitute major obstacles to the large scale usage of PEMFCs. Therefore, for fuel cells it is crucial to lower the value η^{ORR} through the discovery of new catalysts based on earth abundant materials.

In the present study, we use density functional theory (DFT) to determine the Gibbs free energy changes associated with the elementary steps of the OER and ORR occurring on transition metal cations coordinated by porphyrin-like ligands in order to understand the effects of ligand composition on the values of η^{OER} and η^{ORR}. We then explore the possibility of using an axial ligand to further lower the values of η^{OER} and η^{ORR}. Finally, we explore the effect of embedding the porphyrin motif into either graphene sheets or single-walled carbon nanotubes (SWCNTs). Our choice of systems is motivated by a number of relevant experimental studies. First, metal porphyrin complexes and metal corrole complexes (a ring-contracted porphyrin analogue) have been demonstrated as catalysts for the OER[7−11] and ORR.[12,13] For example, Co-5,10,15,20-tetrakis(1,3-dimethylimidazolium-2-yl)porphyrin has been identified as an efficient homogeneous, single-site catalyst for

Received: July 29, 2014
Revised: December 1, 2014
Published: December 15, 2014

   dx.doi.org/10.1021/jp507638v | J. Phys. Chem. C 2014, 118, 29482−29491

water oxidation,[11] and Fe-meso-tetra(pyridyl)porphyrin has been found to be a good electrocatalyst for ORR.[13] Second, metal cations coordinated with porphyrin groups are amenable to a wide range of chemical modifications that can be explored as a means for minimizing η^{OER} and η^{ORR}. Third, the investigation of graphene and carbon nanotubes as supports for OER and ORR catalysts is motivated by recent reports of the effectiveness of these materials for OER[14−17] and ORR.[18−20] We also note that it has recently been shown that nanostructured carbons,[21−23] graphene,[24,25] and carbon nanotubes[26,27] containing Fe cations in porphyrin-like motifs can function as active catalysts for the ORR.

The remainder of the paper is organized as follows. We first introduce the OER and ORR mechanism, the computational standard hydrogen electrode model, and the method for calculating η^{OER} and η^{ORR}. Next, we investigate the use of organometallic complexes as models to identify strategies for reducing η^{OER} and η^{ORR}. Finally, those strategies are applied to graphene and SWCNTs in an attempt to understand how these host materials affect the values of η^{OER} and η^{ORR} of Fe cations held in porphyrin-like ligands and modified with various axial ligands.

2. COMPUTATIONAL DETAILS

For organometallic complexes, geometry optimizations were carried out using the PBE functional[28] with the 6-31G** basis set[29,30] for all atoms except the metal cation. For metal cations we used the small-core, angular-momentum-projected, effective-core potential (ECP) from Los Alamos,[31] for which the outer core and valence electrons are described explicitly using the double-ζ contraction of valence functions.

To obtain the most accurate energetics, we performed single-point energy calculations on previously geometry-optimized structures using the same functional but with a larger basis set: metals were described with the triple-ζ contraction of valence functions augmented with one f-functions[32] but with the core electrons described by the same small core ECP; while the other atoms are described with the 6-311++G** basis set.[33,34] For each system, all possible spin multiplicities were considered and calculated, but only the most stable one was chosen to form the free energy surface.

It has been suggested that the use of functionals including on-site Coulomb repulsion is crucial for predicting η^{OER} and η^{ORR}.[35,36] Therefore, we recalculated the important results using B3LYP[37−39] with the same basis sets and procedure as those for PBE (Tables S2 and S3, Supporting Information). We found that the trends (the correlation between $\Delta\Delta G$ and the group number, and axial ligand effect to η^{OER} and η^{ORR}) in our results are functional-independent. All the cluster calculations were performed using Q-Chem.[40]

For systems with periodic boundary conditions (graphene and CNT), the DFT calculations were performed with the planewave code VASP[41−44] using projector augmented-wave pseudopotentials[45,46] with the PBE functional. The plane wave energy cutoff was set to 400 eV and the density cutoff was set to 700 eV, and electron smearing was employed using the Gaussian-smearing technique with a width of k_BT = 0.1 eV. All calculated values of energies have been extroplated to k_BT = 0. A Monkhorst−Pack k-point grid of 2 × 2 × 1 was chosen to sample the reciprocal space for the graphene systems, whereas for the CNT systems only the gamma point is sampled because of the large model we used (17.04 Å along the tube direction). At least 10 Å vacuum space between adjacent images was used to prevent the interaction between the replicas along the z-direction for graphene and the x- and y-direction for CNT. All the graphene and CNT systems were calculated using the spin-polarized wave functions. We calculated all possible spin states for each system by constraining the difference between the number of α- and β-electrons to range from 0 to 5, and only the most stable one was used to construct the free energy diagram. To convert electronic energies into Gibbs free energies, zero-point energy (ZPE), enthalpic, and entropic corrections and solvation energies are needed. We used the numbers reported by Rossmeisl et al.[47] for ZPE and thermo corrections and those from Koper et al.[48,49] for the solvation correction (Table S1). We also used the dispersion-corrected[50] PBE (PBE-D2) functional to reexamine some important cases (Table S4), and we found that the major conclusions are the same.

We emphasize that this is a purely thermodynamic study, which means no kinetic barriers are calculated or included in the Gibbs free energy surfaces. This simple thermodynamic analysis has been shown to satisfactorily predict experimental overpotentials for other electrocatalytic reactions,[47,51] and the thermodynamic overpotentials provided here represent the lower bounds to the kinetic ones. Moreover, recent computational studies have shown that the kinetic barriers are small and thus surmountable at room temperature.[52−54]

3. RESULTS AND DISCUSSION

3.1. Factors Affecting η^{OER}. The following four-step mechanism, which is supported by the recent ambient-pressure X-ray photoelectron spectroscopy,[55] was used to analyze the thermodynamic aspects of the oxygen evolution reaction and to determine the overpotential for the OER.[56]

$$H_2O_{(l)} + * \rightleftarrows *OH + H^+ + e^-$$

$$\Delta G_1 = \Delta G_{*OH} - eU + k_BT \ln[H^+] \quad (I)$$

$$*OH \rightleftarrows *O + H^+ + e^-$$

$$\Delta G_2 = \Delta G_{*O} - \Delta G_{*OH} - eU + k_BT \ln[H^+] \quad (II)$$

$$*O + H_2O(l) \rightleftarrows *OOH + H^+ + e^-$$

$$\Delta G_3 = \Delta G_{*OOH} - \Delta G_{*O} - eU + k_BT \ln[H^+] \quad (III)$$

$$*OOH \rightleftarrows * + O_2(g) + H^+ + e$$

$$\Delta G_4 = 4.92 - \Delta G_{*OOH} - eU + k_BT \ln[H^+] \quad (IV)$$

In the above steps, the symbol * represents an oxygen vacancy on the catalyst surface, and *OH, *O, and *OOH represent chemisorbed OH, O, and OOH, respectively.

The computational standard hydrogen electrode model proposed by Nørskov and co-workers was used to calculate potential- and pH-dependent free energy surfaces.[57] In the context of this model, the free energy of a proton and an electron is equal to half the free energy of $H_2(g)$ at an applied electric potential U = 0 V vs SHE and pH = 0. The free energy surfaces presented and discussed in this work are at standard conditions (pH = 0, T = 298.15 K) and U = 0 V vs SHE. ΔG_{*OH}, ΔG_{*O}, and ΔG_{*OOH} are the Gibbs free energies of *OH, *O, and *OOH, respectively, referenced to a surface with an oxygen vacancy site (*), $H_2O(l)$, and $H_2(g)$. It is noted that this approach applies equally well to the OER carried out in acidic or basic electrolytes.[58]

dx.doi.org/10.1021/jp507638v | J. Phys. Chem. C 2014, 118, 29482−29491

The computational overpotential, η^{OER}, is defined as the difference between the water equilibrium potential (1.23 V vs SHE) and the potential needed to overcome the most uphill reaction of the four steps. For all OER catalysis considered here, the potential determining step is either reaction II or III,[56] from which it follows that

$$\eta^{OER} = \{\max[\Delta G_2, \Delta G_3]\}/e - 1.23$$
$$= \{\max[(\Delta G_{*O} - \Delta G_{*OH}), (\Delta G_{*OOH} - \Delta G_{*O})]\}/e - 1.23$$
$$= \{\max[(\Delta G_{*O} - \Delta G_{*OH}), (\Delta G_{*OOH} - \Delta G_{*OH}) - (\Delta G_{*O} - \Delta G_{*OH})]\}/e - 1.23$$
$$= \{\max[(\Delta G_{*O} - \Delta G_{*OH}), \Delta\Delta G - (\Delta G_{*O} - \Delta G_{*OH})]\}/e - 1.23 \quad (1)$$

This means that η^{OER} is determined by two factors (as shown in Scheme 1): (a) the difference in Gibbs free energies between *OOH and *OH, ($\Delta\Delta G = \Delta G_{*OOH} - \Delta G_{*OH}$), and (b) the relative position of the Gibbs free energy of *O (ΔG_{*O} - ΔG_{*OH}).

Scheme 1. Schematic description of the Gibbs free energy surface for the oxygen evolution reaction, showing the conventional value of 3.2 V for $\Delta\Delta G$

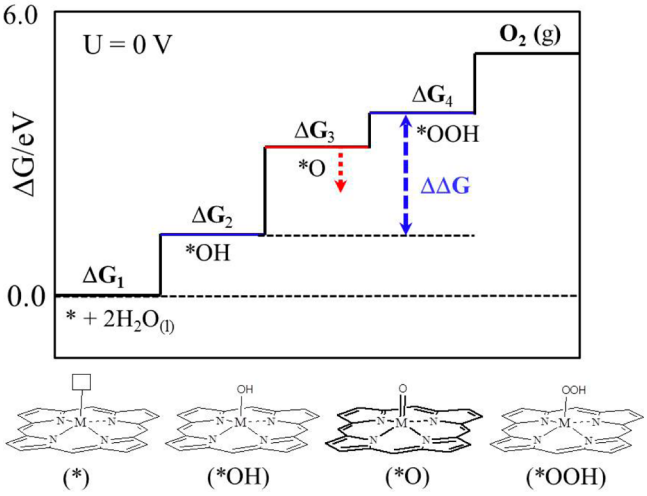

The perfect OER catalyst would have $\Delta\Delta G$ = 2.46 eV and ($\Delta G_{*O} - \Delta G_{*OH}$) = 1.23 eV, leading to η^{OER} = 0 V. However, as proposed by Nørskov and co-workers[56] and Koper,[59] $\Delta\Delta G$ is typically around 3.2 eV, and as a result η^{OER} is almost solely dependent on ($\Delta G_{*O} - \Delta G_{*OH}$) alone. This leads to an intrinsic minimum value for η^{OER} of 0.37 V (3.2 ÷ 2 − 1.23 = 0.37), even when ΔG_{*O} is positioned in the middle of ΔG_{*OOH} and ΔG_{*OH}. Indeed, recent experiments show there exists a lower limit for η^{OER} among all known OER catalysts.[3] In order to achieve lower values of η^{OER}, strategies are needed (i) to obtain values of $\Delta\Delta G$ lower than 3.2 eV and (ii) to position the value of ΔG_{*O} half way between the values of ΔG_{*OOH} and ΔG_{*OH}.

3.2. Reduction of $\Delta\Delta G$. The two ligand motifs shown in Scheme 2 were selected for analysis: (a) six- and five-coordinated metal porphyrin complexes (**Por-6-M** and **Por-5-M**), chosen to represent porphyrin-like motifs that can be

Scheme 2. Porphyrin (Por) Complexes That Represent the Surface Motifs of OER and ORR Electrocatalysts[a]

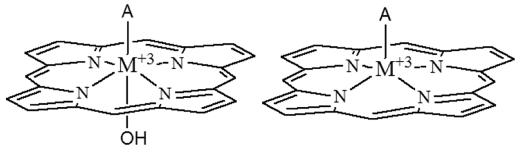

Por-6-M **Por-5-M**

M = Ti, V, Cr, Mn, Fe, Co, Ni
A = *, OH, O, OOH

[a]The resulting overpotential for ORR and OER will vary with choice of the central metal ion (M).

embedded in carbon nanostructures such as graphene[24] and CNTs.[26] Only first-row transition metals (Ti, V, Cr, Mn, Fe, Co, and Ni) were considered, since they are earth abundant and inexpensive.

Values of $\Delta\Delta G$ for **Por-5-M** and **Por-6-M** were calculated. As shown in Table 1, metals on the right-hand side of the

Table 1. $\Delta G_{*OOH} - \Delta G_{*OH}$ ($\Delta\Delta G$) for Five- and Six-Coordinated Metal Porphyrin Complexes[a]

metal	Por-5-M	Por-6-M
Ti	3.37	3.23
V	*b*	3.24
Cr	3.22	3.16
Mn	3.16	3.13
Fe	2.97	2.99
Co	2.93	3.01
Ni	2.80	2.98
R^2	**0.97**	**0.91**

[a]The table also lists the correlation between metal group number with $\Delta G_{*OOH} - \Delta G_{*OH}$. The unit for energy is eV. [b]We were unable to acquire the number for the vanadium case, because during the geometry optimization the *OOH intermediate decomposes into an *O intermediate and a weakly bound OH radical.

periodic table exhibit the lowest values of $\Delta\Delta G$. This trend is similar to that observed in other recent computational studies for metal oxides.[48,49,60,61] A significant finding is that by choice of a metal from the right side of the transition series, we can move closer to the optimal value of $\Delta\Delta G$ = 2.46 V, which opens the possibility of reducing the minimum overpotential ($\eta^{OER} = \Delta\Delta G \div 2 - 1.23$) below the limiting value of η^{OER} = 0.37 V associated with the standard value of $\Delta\Delta G$ = 3.2 V.

The correlation (R^2) between the metal group number and $\Delta\Delta G$ is 0.97 for **Por-5-M** and 0.91 for **Por-6-M**. The origin of the good correlations is likely the greater electronegativity of the OH radical (gas phase EA = 1.83 V) relative to the OOH radical (gas phase EA = 1.08 V).[62] As we go across the series, the M^{3+} metal centers become less readily oxidizable, which destabilizes *OH more than *OOH, leading to smaller values of $\Delta\Delta G$. This is also evidenced by the increasing value of ΔG_{*OH} and experimentally determined redox potentials for the M^{+2}/M^{+3}–OH pair.[63]

In summary, our numerical results, in line with qualitative electronegativity arguments, suggest that more active OER catalysts result when the metallic center is chosen from the

dx.doi.org/10.1021/jp507638v | J. Phys. Chem. C 2014, 118, 29482−29491

Table 2. OER Gibbs Free Energy Surfaces, Binding Energies for OH, O, and OOH Adsorbates and OER and ORR Overpotentials for Por-5-M (M = Ti, Cr, Mn, Fe, Co, and Ni)[a]

M	ΔG_{*OH}	ΔG_{*O}	ΔG_{*OOH}	$\Delta\Delta G$	ΔG_1	ΔG_2	ΔG_3	ΔG_4	η^{OER}
Ti	−1.81	−1.92	1.56	3.37	−1.81	−0.11	3.48	3.36	2.25
Cr	0.22	1.04	3.44	3.22	0.22	0.82	2.40	1.48	1.17
Mn	0.55	1.49	3.71	3.16	0.55	0.94	2.22	1.21	0.99
Fe	0.72	1.64	3.69	2.97	0.72	0.92	2.05	1.23	0.82
Co	1.05	2.78	3.98	2.93	1.05	1.73	1.20	0.94	0.50
Ni	1.99	4.04	4.79	2.80	1.99	2.05	0.75	0.13	0.82

[a]The unit for energy is eV.

right-hand side of the first-row transition metal series, so that the intrinsic value of η^{OER} can be reduced from 0.37 V.

3.3. Factors Influencing the Value of ΔG_{*O}. The reaction energy for each elementary step as well as the corresponding η^{OER} is given in Table 2 for different metals. Our results show that the Co porphyrin complex exhibits the lowest value of η^{OER} consistent with experimental observations[9,11] and previous theoretical studies.[48,49,64] Table 2 also shows that there is a dramatic increase (1.14 eV) in the value ΔG_{*O} going from Fe to Co. This is due to the occupation of M−Oxo σ^* orbitals, significantly weakening the metal−oxo bond order, and is consistent with the fact that metal oxo complexes with more than four *d*-electrons are highly unstable and rare.[65,66]

Figure 1 shows the scaling relations between ΔG_{*OH}, ΔG_{*O}, and ΔG_{*OOH} as a function of ΔG_{*OH} for **Por-5-M**, from which

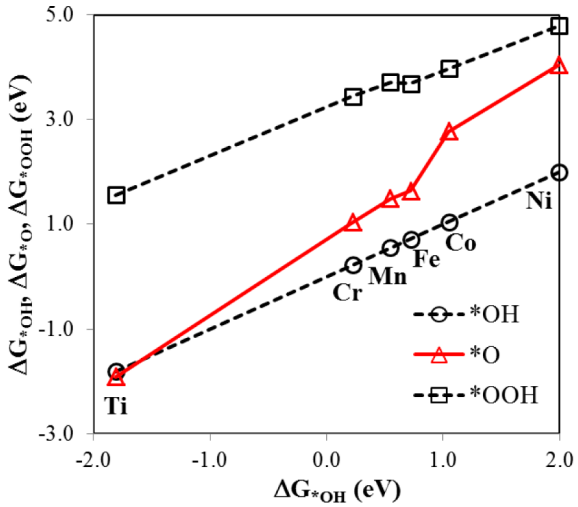

Figure 1. Scaling relations between the adsorption energies of the three OER adsorbates on **Por-5-M** (M = Ti, Cr, Mn, Fe, Co, Ni), *OH (ΔG_{*OH}), *O (ΔG_{*O}), and *OOH (ΔG_{*OOH}) are plotted against the value of ΔG_{*OH}.

we find that the position of ΔG_{*O} relative to the positions of ΔG_{*OH} and ΔG_{*OOH} cannot be fixed precisely half way between the latter two free energies simply by changing the metal center. For instance, when the metallic center is Fe, ΔG_{*O} is too close to ΔG_{*OH} and Reaction III is the potential-determining step: η^{OER} = 0.82 V. To reduce η^{OER}, Fe can be replaced by Co; however, in this case ΔG_{*O} increases too much and becomes too close to ΔG_{*OOH}, so the potential-determining step is Reaction II leading to η^{OER} = 0.50 V. The steeper increase of ΔG_{*O} relative to ΔG_{*OOH} can also be rationalized on the grounds of its greater electronegativity. This means that simply changing the metal cation in a given complex does not give sufficient control of ΔG_{*O}, and hence is not an adequate means for minimizing η^{OER}.

To minimize η^{OER}, it is important to identify means for more precise control of the position of ΔG_{*O} on the free energy diagram. For metal porphyrin complexes, it is well-known that the axial ligand influences catalytic activity[67,68] and selectivity.[69−71] For example, axial ligands markedly affect the reactivity of iron−oxo porphyrin π-cation radicals in olefin epoxidation and alkane hydroxylation.[67] We show below that the values of both η^{OER} and η^{ORR} can be tuned by choice of the axial ligand.

We used **Por-5-Fe** as a model catalyst because graphene[24] and CNTs[26] containing Fe cations in a porphyrin-like motif have been shown to be effective catalysts for the oxygen reduction reaction (ORR). Since the electrochemical oxidation of water takes place in aqueous solution, it is reasonable to assume that in the absence of strongly bound ligands the axial position (**X**, Scheme 3a) would be occupied by water (**Por-5-Fe-H_2O**). Therefore, **Por-5-Fe-H_2O** was used as the reference. Eight different axial ligands including X = H_2O, NMe_3, PH_3, PMe_3, **A**, **B**, **C**, and CO were investigated, since Fe (and other transition metals) porphyrin complexes containing such axial ligands have been described in the literature.[72−76]

Scheme 3. (a) Models for Investigating the Effect of Axial Ligands and (b) Three Model N-Heterocyclic Carbenes Used as Axial Ligands

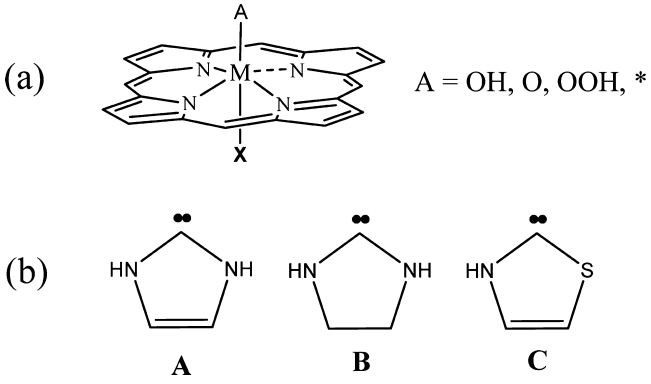

The value of η^{OER} of **Por-5-Fe-H_2O** is 0.75 V with reaction III acting as the potential-determining step (see Table 3). We find that by changing the composition of the axial ligand, η^{OER} can be reduced by as much as 0.48 V: replacing H_2O with **X** = NMe_3, PH_3, PMe_3, **A**, **B**, **C** (Scheme 3b), and CO reduces η^{OER} to 0.66, 0.53, 0.43, 0.35, 0.33, 0.29, and 0.27 V, respectively.

The improvement in OER activity can be rationalized by plotting the values of ΔG_{*OH}, ΔG_{*O}, and ΔG_{*OOH} of **Por-5-Fe-X** versus ΔG_{*OH} (see Figure 2). We find that replacement of H_2O by others axial ligands increases the values of ΔG_{*OH} and

dx.doi.org/10.1021/jp507638v | J. Phys. Chem. C 2014, 118, 29482−29491

Table 3. OER Gibbs Free Energy Surfaces, Binding Energies for OH, O, and OOH Adsorbates, and OER and ORR Overpotentials for Por-5-Fe-X (X = H_2O, NMe_3, PH_3, PMe_3, A, B, C, and CO)[a]

X	ΔG_{*OH}	ΔG_{*O}	ΔG_{*OOH}	$\Delta\Delta G$	ΔG_1	ΔG_2	ΔG_3	ΔG_4	η^{OER}	η^{ORR}
H_2O	0.51	1.57	3.56	3.04	0.51	1.06	***1.98***	1.36	0.75	0.72
NMe_3	0.53	1.65	3.54	3.01	0.53	1.12	***1.89***	1.38	0.66	0.70
PH_3	0.65	1.89	3.65	3.00	0.65	1.23	***1.76***	1.27	0.53	0.58
PMe_3	0.73	2.05	3.71	2.97	0.73	1.31	***1.66***	1.21	0.43	0.50
A	0.76	2.18	3.76	3.00	0.76	1.42	***1.58***	1.16	0.35	0.47
B	0.80	2.26	3.82	3.02	0.80	1.46	***1.56***	1.10	0.33	0.43
C	0.83	2.29	3.80	2.97	0.83	1.45	***1.52***	1.12	0.29	0.40
CO	1.22	2.72	4.09	2.87	1.22	***1.50***	1.37	0.83	0.27	0.40

[a]The unit for energy is eV.

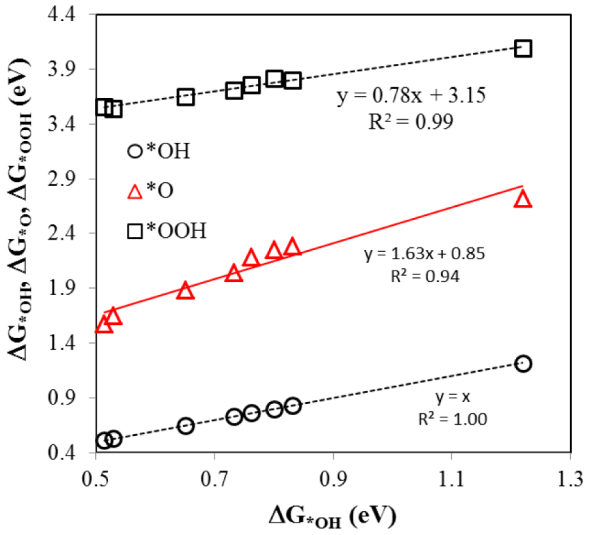

Figure 2. Scaling relations between the adsorption energies of the three OER adsorbates on **Por-5-Fe-X** (**X** = H_2O, NMe_3, PH_3, PMe_3, **A**, **B**, **C**, and CO). The values for *OH (ΔG_{*OH}), *O (ΔG_{*O}), and *OOH (ΔG_{*OOH}) are plotted against the value of ΔG_{*OH}.

ΔG_{*OOH} (see Table 2). Figure 2 shows that ΔG_{*OOH} increases more slowly than ΔG_{*OH} (with a slope of 0.78), whereas ΔG_{*O} increases more rapidly than ΔG_{*OH} (with a slope of 1.63). What this means is that as X is changed from H_2O to CO, the magnitude of $\Delta\Delta G$ decreases and the value of ΔG_{*O} shifts from below the midpoint between ΔG_{*OH} and ΔG_{*OOH} to above the midpoint.

Another way to explain these results is to look at how the four intermediates, *, *OH, *O, and *OOH, are stabilized/destabilized as the composition of the axial ligand is varied from H_2O to CO. We find that the replacement of **X** = H_2O to NMe_3, PH_3, PMe_3, **A**, **B**, **C**, and CO stabilizes *OH and *OOH by a larger and similar amount, whereas it stabilizes (or destabilizes when X = PH_3, and CO) *O only by a smaller amount (Table 4). The outcome of this uneven axial ligand stabilization effect pushes ΔG_{*O} up in the free energy diagram, approaching the middle of ΔG_{*OH} and ΔG_{*OOH} and resulting in a low value of η^{OER}.

3.4. The Effect of Axial Ligands on η^{ORR}. Since ORR is the reverse of OER, we also calculated the ORR overpotential (η^{ORR}) for Fe porphyrin complexes, which is defined as the difference between 1.23 V and the reaction energy of the least uphill of the four mechanistic steps:[77]

$$\eta^{ORR} = 1.23 - \{\min[\Delta G_1, \Delta G_2, \Delta G_3, \Delta G_4]\}/e \quad (2)$$

Table 4. Axial Ligand Exchange Energy for Por-5-Fe-X (X = H_2O, NMe_3, PH_3, PMe_3, A, B, C, and CO)[a]

ligand (X)	E(*)	E(*OH)	E(*O)	E(*OOH)
H_2O	0.00	0.00	0.00	0.00
NMe_3	−0.12	−0.10	−0.04	−0.13
PH_3	−0.18	−0.05	0.13	−0.09
PMe_3	−0.69	−0.48	−0.23	−0.55
A	−1.41	−1.16	−0.80	−1.21
B	−1.48	−1.19	−0.80	−1.22
C	−1.39	−1.08	−0.68	−1.15
CO	−1.04	−0.33	0.11	−0.50

[a]**X** = H_2O was used as the reference. The unit for energy is eV.

As shown in Table 3, we find that the composition of the axial ligand has a significant effect on the value of η^{ORR}, reducing it from 0.72 (**X** = H_2O) to 0.70 (NMe_3), 0.58 (PH_3), 0.50 (PMe_3), 0.47 (**A**), 0.43 (**B**), 0.40 (**C**), and 0.40 V (CO). Consistent with these findings, Anson and co-workers have reported that measured ORR potentials shift to more positive values (i.e., to lower values of η^{ORR}) when Fe porphyrin complexes are attached to a pyrolytic graphite electrode by an axial ligand.[78]

The improvement of ORR activity can also be seen from the data in Table 4. Usually the potential-determining step for ORR is either the reverse of reaction I or II,[77] and therefore eq (2) can be rewritten as

$$\begin{aligned}\eta^{ORR} &= 1.23 - \{\min[\Delta G_1, \Delta G_4]\}/e \\ &= 1.23 - \{\min[\Delta G_{*OH}, 4.92 - \Delta G_{*OOH}]\}/e \\ &= 1.23 - \{\min[\Delta G_{*OH}, 4.92 - \Delta G_{*OH} \\ &\quad - (\Delta G_{*OOH} - \Delta G_{*OH})]\}/e \\ &= 1.23 - \{\min[\Delta G_{*OH}, 4.92 - \Delta G_{*OH} \\ &\quad - (\Delta\Delta G)]\}/e\end{aligned} \quad (3)$$

In the current system $\Delta\Delta G$ is approximately 3.0 eV, and therefore eq (3) can be rewritten as

$$\begin{aligned}\eta^{ORR} &= 1.23 - \{\min[\Delta G_{*OH}, 4.92 - \Delta G_{*OH} - 3.0]\}/e \\ &= 1.23 - \{\min[\Delta G_{*OH}, 1.92 - \Delta G_{*OH}]\}/e\end{aligned} \quad (4)$$

This means that the catalyst ORR activity depends only on ΔG_{*OH}, the adsorbed OH formation energy referenced to a vacant site (*), $H_{2(g)}$, and $H_2O_{(l)}$. For **X** = H_2O, ΔG_{*OH} is only 0.51 eV, which leads to a large η^{ORR} of 0.72 V. This number is

dx.doi.org/10.1021/jp507638v | J. Phys. Chem. C 2014, 118, 29482−29491

far smaller than the optimal ΔG_{*OH} of 0.96 (= 1.92 ÷ 2) V, which would lead to η^{ORR} = 0.27 V. As shown in the first two columns of Table 4, replacing H_2O with NMe_3, PH_3, PMe_3, **A**, **B**, **C**, and CO stabililizes vacant site (*) intermediate more than the *OH intermediate. This weakens the bond between OH and the surface, increases ΔG_{*OH}, and reduces η^{ORR}.

3.5. Graphene and Carbon Nanotube Systems. The idea of using an axial ligand to adjust the values of η^{OER} and η^{ORR} for a Fe cation coordinated to a porphyrin-like moiety embedded in a graphene sheet (**G-Fe-X**) or a single-walled carbon nanotube (**SWCNT-Fe-X**) was examined in the next phase of our work. Illustrations of the structures are shown in Scheme 4. This part of our effort was motivated by extensive studies of **G-Fe** and **SWCNT-Fe** for the ORR.[24,26] Table 5 shows that for **G-Fe-X** the choice of axial ligand enables delicate control of the related position of ΔG_{*O} in the free energy diagram in a manner similar to that observed for the porphyrin systems. Importantly, we observe that by selection of the axial ligand the value of η^{OER} can be reduced from 0.78 V for X = H_2O to 0.35 V for X = **C**. We note that the potential-determining step changes from Reaction III for X = H_2O, NMe_3, PH_3, PMe_3, **A**, and **B** to Reaction II for X = **C** and CO. This means that when X = **B** and **C** the OER activity of the catalyst reaches the top of the volcano plot. Selection of the axial ligand can also reduce the value of η^{ORR} from 0.68 V for X = H_2O to 0.37 V for **X** = PH_3.

Scheme 4. (a) Model for the Graphene G-Fe-H_2O Surface Formed from One Fe, Four N, and 26 C plus an Axial Ligand H_2O and a OH Adsorbate; (b) Model for SWCNT^{OUT}-Fe-H_2O (CNT(14,0)) consisting of One Fe, Four N, and 218 C plus a OH Adsorbate and an Axial Ligand H_2O That Binds with Fe Inside the Tube; (c) Model for SWCNT^{IN}-Fe-H_2O Consisting of One Fe, Four N, and 218 C plus a OH Adsorbate and an Axial Ligand H_2O That Binds with Fe Outside the Tube

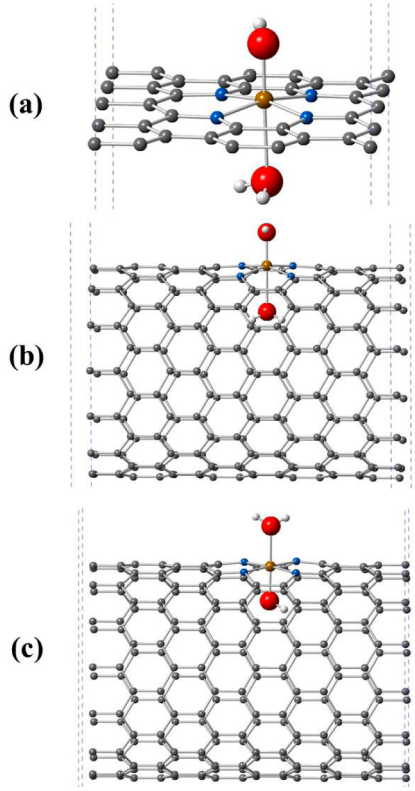

In the case of SWCNTs, it is possible to place the axial ligand inside or outside the nanotube with the consequence that the OER or ORR can occur outside or inside the nanotube (see Scheme 4, parts b and c). We refer to these cases as catalysis outside, **SWCNT^{OUT}-Fe-X** (i.e., Scheme 4b), and catalysis inside, **SWCNT^{IN}-Fe-X** (i.e., Scheme 4c). The results for both cases are summarized in Table 6. Only **X** = H_2O, PMe_3, **A**, **B**, **C**, and CO are considered, since in the metal porphyrin and graphene systems only these ligands improved OER and ORR activity significantly.

For **SWCNT^{OUT}-Fe-X**, replacing **X** = H_2O with PMe_3 increases η^{OER} from 0.75 to 0.84 V, but decreases η^{ORR} from 0.82 to 0.66 V. This small effect (relative to the results of the previous section) for interior PMe_3 may be due to steric repulsion with the carbon wall of the tube weakening the axial ligand interaction with the metal. In fact, R(Fe-PMe_3) is calculated to be 2.64 Å for the *OH intermediate of **SWCNT^{OUT}-Fe-PMe_3**, which is much larger than that for **G-Fe-PMe_3** (2.37 Å). By contrast, CO, **B**, and **C** significantly reduce the value of η^{OER} to 0.39, 0.36, and 0.36 V, respectively and reduce the value of η^{ORR} to 0.31, 0.53, and 0.54 V, respectively. It is not surprising that CO has a significant axial ligand effect, since it is small enough to ligate with the Fe center without experiencing significant steric repulsion. Indeed, we observe that R(Fe-CO) = 1.79 Å for the *OH intermediate in **SWNT^{OUT}-Fe-CO** which is the same as that for **G-Fe-CO**. The effectiveness of the model heterocyclic carbenes, **B** and **C**, is also a consequence of the relatively small size of these ligands. We find R(Fe−**B**) = 2.12 Å and R(Fe−**C**) = 2.01 Å for the *OH intermediates, values that are comparable to those for **G-Fe-B** (1.97 Å) and **G-Fe-C** (1.96 Å).

For catalysis within the nanotube, **SWCNT^{IN}-Fe-X**, we find that X = **A**, **B**, **C**, and even PMe_3 cause a significant reduction in the η^{OER} from 0.88 V for H_2O to 0.41, 0.37, 0.35, and 0.40 V, respectively. The reason that PMe_3 gives larger improvement in the OER activity than for **SWNT^{OUT}-Fe-PMe_3** is stronger interaction of the ligand with the Fe center. Indeed, R(Fe-PMe_3) = 2.23 Å for the *OH intermediate in **SWNT^{OUT}-Fe-PMe_3**, which is much shorter than that for **SWCNT^{IN}-Fe-PMe_3** (2.64 Å) and even shorter than that of **G-Fe-PMe_3** (2.37 Å).

In contrast to **G-Fe-X** and **SWCNT^{OUT}-Fe-X**, the replacement of X = H_2O in **SWNT^{IN}-Fe-X** by PMe_3, **A**, **C**, or CO causes small reductions in the value of η^{ORR} (η^{ORR} = 0.45 V for H_2O, η^{ORR} = 0.37 for PMe_3, η^{ORR} = 0.42 for **A**, η^{ORR} = 0.43 for **C**, and η^{ORR} = 0.38 for CO), and replacement by **B** even increases η^{ORR} slightly to 0.46 V. This is because η^{ORR} for **SWCNT^{IN}-Fe-H_2O** is already low, compared to the case of **SWCNT^{OUT}-Fe-H_2O**. As shown in eq (4), η^{ORR} depends on ΔG_{*OH}. For **SWCNT^{OUT}-Fe-H_2O**, ΔG_{*OH} is only 0.41 eV, leading to a η^{ORR} = 0.82 V, leaving considerable room for improvement. By contrast, for **SWCNT^{IN}-Fe-H_2O**, repulsion between adsorbed OH and the wall of the nanotube increases ΔG_{*OH} to 0.78 eV and therefore η^{ORR} decreases to 0.45 V, leaving much less room for improvement. The repulsion is evidenced by the increase in R(Fe−OH) from 1.79 Å for **SWCNT^{OUT}-Fe-H_2O** to 1.85 Å for **SWCNT^{IN}-Fe-H_2O**.

On the basis of the results reported above, we propose two novel designs of electrocatalyst for OER and ORR. Our first design comprises a metal porphyrin-like moiety embedded into a carbon nanotube and a bulky ligand occupying the axial site on the outside of the tube (Figure 3a). In this case, catalysis can

dx.doi.org/10.1021/jp507638v | J. Phys. Chem. C 2014, 118, 29482−29491

Table 5. OER Gibbs Free Energy Surfaces, Binding Energies for OH, O, and OOH Adsorbates, and OER and ORR Overpotentials for G-Fe-X (X = H_2O, NMe_3, PH_3, PMe_3, A, B, C, and CO)[a]

X	ΔG_{*OH}	ΔG_{*O}	ΔG_{*OOH}	$\Delta\Delta G$	ΔG_1	ΔG_2	ΔG_3	ΔG_4	η^{OER}	η^{ORR}
H_2O	0.55	1.56	3.56	3.01	0.55	1.01	***2.01***	1.36	0.78	0.68
NMe_3	0.66	1.70	3.69	3.02	0.66	1.04	***1.98***	1.23	0.75	0.57
PH_3	1.04	2.07	4.06	3.02	1.04	1.03	***2.00***	0.86	0.77	0.37
PMe_3	1.04	2.40	4.07	3.04	1.04	1.36	***1.68***	0.85	0.45	0.38
A	0.90	2.44	4.15	3.25	0.90	1.54	***1.71***	0.77	0.48	0.46
B	0.97	2.52	4.12	3.15	0.97	1.56	***1.59***	0.80	0.36	0.43
C	1.09	2.67	4.20	3.11	1.09	***1.58***	1.53	0.72	0.35	0.51
CO	1.33	3.18	4.41	3.08	1.33	***1.85***	1.22	0.51	0.62	0.72

[a]The unit for energy is eV.

Table 6. OER Gibbs Free Energy Surfaces, Binding Energies for OH, O, and OOH Adsorbates, and OER and ORR Overpotentials for $SWNT^{OUT}$-X and $SWNT^{IN}$-X (X = H_2O, PMe_3, A, B, C, and CO)[a]

X	ΔG_{*OH}	ΔG_{*O}	ΔG_{*OOH}	$\Delta\Delta G$	ΔG_1	ΔG_2	ΔG_3	ΔG_4	η^{OER}	η^{ORR}
					$SWNT^{OUT}$					
H_2O	0.41	1.34	3.32	2.91	0.41	0.93	1.98	1.60	0.75	0.82
PMe_3	0.57	1.48	3.55	2.98	0.57	0.91	2.07	1.37	0.84	0.66
A	0.58	1.98	3.65	3.07	0.58	1.41	1.67	1.27	0.44	0.65
B	0.70	2.29	3.86	3.15	0.70	1.59	1.57	1.06	0.36	0.53
C	0.69	2.09	3.68	2.99	0.69	1.40	1.59	1.24	0.36	0.54
CO	0.92	2.54	4.00	3.08	0.92	1.62	1.46	0.92	0.39	0.31
					$SWNT^{IN}$					
H_2O	0.78	1.79	3.89	3.11	0.78	1.00	2.11	1.03	0.88	0.45
PMe_3	1.00	2.43	4.06	3.06	1.00	1.44	1.63	0.86	0.40	0.37
A	1.01	2.46	4.11	3.09	1.01	1.45	1.64	0.81	0.41	0.42
B	1.06	2.55	4.15	3.09	1.06	1.49	1.60	0.77	0.37	0.46
C	1.06	2.64	4.12	3.06	1.06	1.58	1.48	0.80	0.35	0.43
CO	0.96	3.12	4.07	3.12	0.96	2.16	0.96	0.85	0.93	0.38

[a]The unit for energy is eV.

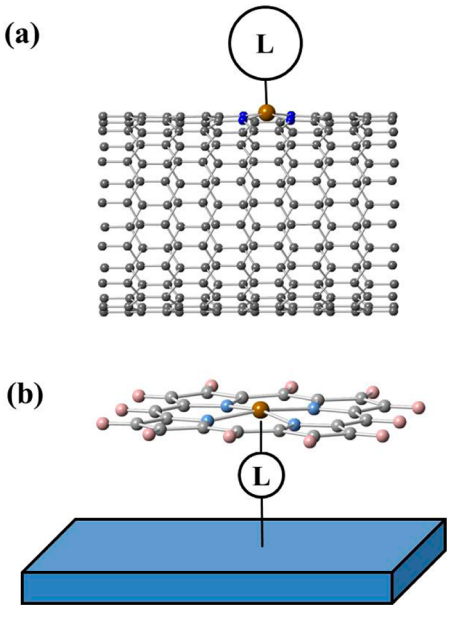

Figure 3. Schematic description of the two noval designs of OER (or ORR) electrocatalyst. The symbol "L" represents the axial ligand.

only occur inside the nanotube architecture and offers several advantages. Strongly interacting ligands such as phosphine and N-heterocyclic carbenes cannot poison the active site, as they can be designed to be too bulky to enter the carbon tube. A second advantage is that water, gas, proton, and ion transport occurs more rapidly inside than outside the tube,[79−86] and therefore the OER and ORR could be accelerated in the transport limited region. However, the embedding of the porphyrin-like motif into the carbon nanotube may change its charge distribution and thus affect the transport efficiency, The second design involves N-heterocyclic carbene ligands or phosphine ligands bound to electrodes through linkers, and coordination of the ligand with metal porphyrin complexes (Figure 3 (b)). This design is similar to what was proposed by Shi and Anson.[78]

4. CONCLUSIONS

Analysis of the OER occurring on first-row transition metal cations contained in metal oxide has shown that the minimum value of the potential-limited overpotential, η^{OER}, is dictated by the value ($\Delta G_{*OOH} - \Delta G_{*OH}$), the difference in the Gibbs free energies for the binding of adsorbed OOH and OH species, *OOH and *OH. For metal oxides the value of (ΔG_{*OOH} - ΔG_{*OH}) is between 3.4 and 3.2 eV, which means that the minimum value of η^{OER} that can be achieved is between 0.47 and 0.37 eV.[56] Therefore, to achieve lower values of η^{OER} requires finding coordination motifs for transition metal cations that provide values of ($\Delta G_{*OOH} - \Delta G_{*OH}$) that lie below 3.2 eV. We show here that values of ($\Delta G_{*OOH} - \Delta G_{*OH}$) between 3.4 and 2.8 can be achieved for first-row transition metal cations coordinated with the porhyrin ligand with the lowest values being for trivalent metal cations occurring to the right-hand side of the first row of transition metal cations (e.g., Co^{3+}, Fe^{3+} and Ni^{3+}).

dx.doi.org/10.1021/jp507638v | J. Phys. Chem. C 2014, 118, 29482−29491

For a given metal cation and ligand, the lowest value of η^{OER} will occur when the value of ΔG_{*O} lies midway between the values for ΔG_{*OOH} and ΔG_{*OH}. Our analysis reveals that for a given cation and ligand system the value of ($\Delta G_{*OOH} - \Delta G_{*OH}$) can be reduced and the value of ΔG_{*O} simultaneously tuned to lie midway between the values for ΔG_{*OOH} and ΔG_{*OH} by proper choice of ligand. Thus, for example, the value of η^{OER} for **Por-5-Fe-H_2O** can be reduced from 0.75 eV when H_2O serves as the axial ligand to as low as 0.27 V, when the CO serves as the axial ligand (i.e., **Por-5-Fe-CO**), which is not much higher than the minimum value for η^{OER}, 0.21 eV. If the porphyrin motif is incorporated into a graphene sheet or into a single-walled carbon nanotube, the lowest value of η^{OER} determined for the ligands considered is ∼0.35 eV using the N-heterocyclic carbene **C** (see Scheme 3) as the axial ligand.

It should be noted that the axial ligand effect can only push ΔG_{*O} up in Gibbs free energy. This helps to reduce η^{OER} for M = Fe, Mn, and Cr, but this does not improve the OER activity for M = Co and Ni, which possess the smallest value of $\Delta\Delta G$ and therefore the smallest intrinsic η^{OER} among the first-row transition metals. This is because for M = Co and Ni, which have more than four *d*-electrons, the oxo intermediates (M^{+4}═O) are highly unstable. To utilize these metals as active sites for OER, some strategy, such as using a π-electron withdrawing ligand or redox-inactive metal ions,[87,88] must be used to stabilize the *O intermediate, thereby making reaction III the potential determining step.

The overpotential for the ORR can also be lowered through the use of axial ligands for the ORR. For example, the value of η^{ORR} can be reduced from 0.72 eV for **Por-5-Fe-H_2O** down to 0.40 eV for **Por-5-Fe-C**. When the porphyrin motif is incorporated into a graphene sheet, the lowest value for η^{ORR} is attained for **G-Fe-PH_3**, 0.37 eV. When the porphyrin motif is incorporated into a single-walled carbon nanotube the lowest value of η^{ORR} is obtained for **SWNT^{out}-Fe-CO**, 0.31 eV. Protecting the active site from poisoning by strongly interacting axial ligands can be accomplished by doing catalysis inside the nanotube, where suitably chosen bulky ligands cannot enter.

In summary, this study has shown that value of η^{OER} significantly lower than those determined for metal oxides and values of η^{ORR} below those determined for Pt (the most active catalyst for ORR) can be achieved by coordinating Fe^{3+}, and other late, first-row transition metal cations, with porphyrin ligands or porphyrin-like ligands incorporated into single-walled carbon nanotubes and an axial ligand.

■ ASSOCIATED CONTENT

Supporting Information

Additional tables and details regarding computational methods. This material is available free of charge via the Internet at http://pubs.acs.org.

■ AUTHOR INFORMATION

Corresponding Authors

*(M.G.-H.) E-mail: mhg@cchem.berkeley.edu. Telephone: +1 510 642 5957.

*(A.T.B.) E-mail: alexbell@berkeley.edu. Telephone: +1 510 642 1536.

Notes

The authors declare no competing financial interest.

■ ACKNOWLEDGMENTS

This material is based on work performed in the Joint Center for Artificial Photosynthesis, a DOE Energy Innovation Hub, supported through the Office of Science of the U.S. Department of Energy under Award Number DE-SC0004993.

■ REFERENCES

(1) Cook, T. R.; Dogutan, D. K.; Reece, S. Y.; Surendranath, Y.; Teets, T. S.; Nocera, D. G. Solar Energy Supply and Storage for the Legacy and Non Legacy Worlds. *Chem. Rev.* **2010**, *110*, 6474−6502.

(2) Walter, M. G.; Warren, E. L.; McKone, J. R.; Boettcher, S. W.; Mi, Q. X.; Santori, E. A.; Lewis, N. S. Solar Water Splitting Cells. *Chem. Rev.* **2010**, *110*, 6446−6473.

(3) McCrory, C. C. L.; Jung, S. H.; Peters, J. C.; Jaramillo, T. F. Benchmarking Heterogeneous Electrocatalysts for the Oxygen Evolution Reaction. *J. Am. Chem. Soc.* **2013**, *135*, 16977−16987.

(4) Steele, B. C. H.; Heinzel, A. Materials for Fuel-Cell Technologies. *Nature* **2001**, *414*, 345−352.

(5) Gasteiger, H. A.; Markovic, N. M. Just a Dream-or Future Reality? *Science* **2009**, *324*, 48−49.

(6) Gasteiger, H. A.; Kocha, S. S.; Sompalli, B.; Wagner, F. T. Activity Benchmarks and Requirements for Pt, Pt-Alloy, and Non-Pt Oxygen Reduction Catalysts for Pemfcs. *Appl. Catal. B: Environ.* **2005**, *56*, 9−35.

(7) Naruta, Y.; Sasayama, M.; Sasaki, T. Oxygen Evolution by Oxidation of Water with Manganese Porphyrin Dimers. *Angew. Chem., Int. Ed.* **1994**, *33*, 1839−1841.

(8) Gao, Y.; Akermark, T.; Liu, J. H.; Sun, L. C.; Akermark, B. Nucleophilic Attack of Hydroxide on a Mn-V Oxo Complex: A Model of the O-O Bond Formation in the Oxygen Evolving Complex of Photosystem II. *J. Am. Chem. Soc.* **2009**, *131*, 8726−8727.

(9) Dogutan, D. K.; McGuire, R.; Nocera, D. G. Electocatalytic Water Oxidation by Cobalt(III) Hangman β-Octafluoro Corroles. *J. Am. Chem. Soc.* **2011**, *133*, 9178−9180.

(10) Nakazono, T.; Parent, A. R.; Sakai, K. Cobalt Porphyrins as Homogeneous Catalysts for Water Oxidation. *Chem. Commun.* **2013**, *49*, 6325−6327.

(11) Wang, D.; Groves, J. T. Efficient Water Oxidation Catalyzed by Homogeneous Cationic Cobalt Porphyrins with Critical Roles for the Buffer Base. *Proc. Natl. Acad. Sci. U.S.A.* **2013**, *110*, 15579−15584.

(12) Su, B.; Hatay, I.; Trojanek, A.; Samec, Z.; Khoury, T.; Gros, C. P.; Barbe, J. M.; Daina, A.; Carrupt, P. A.; Girault, H. H. Molecular Electrocatalysis for Oxygen Reduction by Cobalt Porphyrins Adsorbed at Liquid/Liquid Interfaces. *J. Am. Chem. Soc.* **2010**, *132*, 2655−2662.

(13) Matson, B. D.; Carver, C. T.; Von Ruden, A.; Yang, J. Y.; Raugei, S.; Mayer, J. M. Distant Protonated Pyridine Groups in Water-Soluble Iron Porphyrin Electrocatalysts Promote Selective Oxygen Reduction to Water. *Chem. Commun.* **2012**, *48*, 11100−11102.

(14) Li, F.; Zhang, B. B.; Li, X. N.; Jiang, Y.; Chen, L.; Li, Y. Q.; Sun, L. C. Highly Efficient Oxidation of Water by a Molecular Catalyst Immobilized on Carbon Nanotubes. *Angew. Chem., Int. Ed.* **2011**, *50*, 12276−12279.

(15) Toma, F. M.; Sartorel, A.; Carraro, M.; Bonchio, M.; Prato, M. Dendron-Functionalized Multiwalled Carbon Nanotubes Incorporating Polyoxometalates for Water-Splitting Catalysis. *Pure Appl. Chem.* **2011**, *83*, 1529−1542.

(16) Toma, F. M.; et al. Tailored Functionalization of Carbon Nanotubes for Electrocatalytic Water Splitting and Sustainable Energy Applications. *ChemSusChem* **2011**, *4*, 1447−1451.

(17) Toma, F. M.; et al. Efficient Water Oxidation at Carbon Nanotube-Polyoxometalate Electrocatalytic Interfaces. *Nat. Chem.* **2010**, *2*, 826−831.

(18) Morozan, A.; Campidelli, S.; Filoramo, A.; Jousselme, B.; Palacin, S. Catalytic Activity of Cobalt and Iron Phthalocyanines or Porphyrins Supported on Different Carbon Nanotubes Towards Oxygen Reduction Reaction. *Carbon* **2011**, *49*, 4839−4847.

(19) Kruusenberg, I.; Mondal, J.; Matisen, L.; Sammelselg, V.; Tammeveski, K. Oxygen Reduction on Graphene-Supported Mn_4

Macrocycles in Alkaline Media. *Electrochem. Commun.* **2013**, *33*, 18−22.
(20) Elouarzaki, K.; Le Goff, A.; Holzinger, M.; Thery, J.; Cosnier, S. Electrocatalytic Oxidation of Glucose by Rhodium Porphyrin-Functionalized Mwcnt Electrodes: Application to a Fully Molecular Catalyst-Based Glucose/O_2 Fuel Cell. *J. Am. Chem. Soc.* **2012**, *134*, 14078−14085.
(21) Jaouen, F.; Marcotte, S.; Dodelet, J. P.; Lindbergh, G. Oxygen Reduction Catalysts for Polymer Electrolyte Fuel Cells from the Pyrolysis of Iron Acetate Adsorbed on Various Carbon Supports. *J. Phys. Chem. B* **2003**, *107*, 1376−1386.
(22) Lefevre, M.; Dodelet, J. P.; Bertrand, P. Molecular Oxygen Reduction in PEM Fuel Cell Conditions: ToF-SIMS Analysis of Co-Based Electrocatalysts. *J. Phys. Chem. B* **2005**, *109*, 16718−16724.
(23) Lefevre, M.; Dodelet, J. P.; Bertrand, P. Molecular Oxygen Reduction in PEM Fuel Cells: Evidence for the Simultaneous Presence of Two Active Sites in Fe-Based Catalysts. *J. Phys. Chem. B* **2002**, *106*, 8705−8713.
(24) Lefevre, M.; Proietti, E.; Jaouen, F.; Dodelet, J. P. Iron-Based Catalysts with Improved Oxygen Reduction Activity in Polymer Electrolyte Fuel Cells. *Science* **2009**, *324*, 71−74.
(25) Fu, X. G.; Liu, Y. R.; Cao, X. P.; Jin, J. T.; Liu, Q.; Zhang, J. Y. FeCo-N_x Embedded Graphene as High Performance Catalysts for Oxygen Reduction Reaction. *Appl. Catal., B* **2013**, *130*, 143−151.
(26) Lee, D. H.; Lee, W. J.; Lee, W. J.; Kim, S. O.; Kim, Y. H. Theory, Synthesis, and Oxygen Reduction Catalysis of Fe-Porphyrin-Like Carbon Nanotube. *Phys. Rev. Lett.* **2011**, *106*.
(27) Yang, J. B.; Liu, D. J.; Kariuki, N. N.; Chen, L. X. Aligned Carbon Nanotubes with Built-in FeN_4 Active Sites for Electrocatalytic Reduction of Oxygen. *Chem. Commun.* **2008**, 329−331.
(28) Perdew, J. P.; Burke, K.; Ernzerhof, M. Generalized Gradient Approximation Made Simple. *Phys. Rev. Lett.* **1996**, *77*, 3865−3868.
(29) Francl, M. M.; Pietro, W. J.; Hehre, W. J.; Binkley, J. S.; Gordon, M. S.; Defrees, D. J.; Pople, J. A. Self-Consistent Molecular-Orbital Methods 0.23. A Polarization-Type Basis Set for 2nd-Row Elements. *J. Chem. Phys.* **1982**, *77*, 3654−3665.
(30) Hehre, W. J.; Ditchfie, R.; Pople, J. A. Self-Consistent Molecular-Orbital Methods 0.12. Further Extensions of Gaussian-Type Basis Sets for Use in Molecular-Orbital Studies of Organic-Molecules. *J. Chem. Phys.* **1972**, *56*, 2257−2261.
(31) Hay, P. J.; Wadt, W. R. Ab initio Effective Core Potentials for Molecular Calculations - Potentials for K to Au Including the Outermost Core Orbitals. *J. Chem. Phys.* **1985**, *82*, 299−310.
(32) Ehlers, A. W.; Bohme, M.; Dapprich, S.; Gobbi, A.; Hollwarth, A.; Jonas, V.; Kohler, K. F.; Stegmann, R.; Veldkamp, A.; Frenking, G. A Set of f-Polarization Functions for Pseudo-Potential Basis-Sets of the Transition-Metals Sc-Cu, Y-Ag and La-Au. *Chem. Phys. Lett.* **1993**, *208*, 111−114.
(33) Krishnan, R.; Binkley, J. S.; Seeger, R.; Pople, J. A. Self-Consistent Molecular-Orbital Methods 0.20. Basis Set for Correlated Wave-Functions. *J. Chem. Phys.* **1980**, *72*, 650−654.
(34) Clark, T.; Chandrasekhar, J.; Spitznagel, G. W.; Schleyer, P. V. Efficient Diffuse Function-Augmented Basis Sets for Anion Calculations. Iii. The 3-21+G Basis Set for First-Row Elements, Li-F. *J. Comput. Chem.* **1983**, *4*, 294−301.
(35) Garcia-Mota, M.; Bajdich, M.; Viswanathan, V.; Vojvodic, A.; Bell, A. T.; Nørskov, J. K. Importance of Correlation in Determining Electrocatalytic Oxygen Evolution Activity on Cobalt Oxides. *J. Phys. Chem. C* **2012**, *116*, 21077−21082.
(36) Wang, Y.; Cheng, H. P. Oxygen Reduction Activity on Perovskite Oxide Surfaces: A Comparative First-Principles Study of $LaMnO_3$, $LaFeO_3$, and $LaCrO_3$. *J. Phys. Chem. C* **2013**, *117*, 2106−2112.
(37) Lee, C. T.; Yang, W. T.; Parr, R. G. Development of the Colle-Salvetti Correlation-Energy Formula into a Functional of the Electron-Density. *Phys. Rev. B* **1988**, *37*, 785−789.
(38) Becke, A. D. Density-Functional Thermochemistry 0.3. The Role of Exact Exchange. *J. Chem. Phys.* **1993**, *98*, 5648−5652.
(39) Becke, A. D. Density-Functional Exchange-Energy Approximation with Correct Asymptotic-Behavior. *Phys. Rev. A* **1988**, *38*, 3098−3100.
(40) Shao, Y.; Molnar, L. F.; Jung, Y.; Kussmann, J.; Ochsenfeld, C.; Brown, S. T.; Gilbert, A. T. B.; Slipchenko, L. V.; Levchenko, S. V.; O'Neill, D. P.; et al. Advances in Methods and Algorithms in a Modern Quantum Chemistry Program Package. *Phys. Chem. Chem. Phys.* **2006**, *8*, 3172−3191.
(41) Kresse, G.; Furthmuller, J. Efficiency of Ab-Initio Total Energy Calculations for Metals and Semiconductors Using a Plane-Wave Basis Set. *Comput. Mater. Sci.* **1996**, *6*, 15−50.
(42) Kresse, G.; Furthmuller, J. Efficient Iterative Schemes for Ab Initio Total-Energy Calculations Using a Plane-Wave Basis Set. *Phys. Rev. B* **1996**, *54*, 11169−11186.
(43) Kresse, G.; Hafner, J. Abinitio Molecular-Dynamics for Liquid-Metals. *Phys. Rev. B* **1993**, *47*, 558−561.
(44) Kresse, G.; Hafner, J. Ab-Initio Molecular-Dynamics Simulation of the Liquid-Metal Amorphous-Semiconductor Transition in Germanium. *Phys. Rev. B* **1994**, *49*, 14251−14269.
(45) Blochl, P. E. Projector Augmented-Wave Method. *Phys. Rev. B* **1994**, *50*, 17953−17979.
(46) Kresse, G.; Joubert, D. From Ultrasoft Pseudopotentials to the Projector Augmented-Wave Method. *Phys. Rev. B* **1999**, *59*, 1758−1775.
(47) Rossmeisl, J.; Qu, Z. W.; Zhu, H.; Kroes, G. J.; Nørskov, J. K. Electrolysis of Water on Oxide Surfaces. *J. Electroanal. Chem.* **2007**, *607*, 83−89.
(48) Calle-Vallejo, F.; Martinez, J. I.; Garcia-Lastra, J. M.; Abad, E.; Koper, M. T. M. Oxygen Reduction and Evolution at Single-Metal Active Sites: Comparison between Functionalized Graphitic Materials and Protoporphyrins. *Surf. Sci.* **2013**, *607*, 47−53.
(49) Calle-Vallejo, F.; Martinez, J. I.; Rossmeisl, J. Density Functional Studies of Functionalized Graphitic Materials with Late Transition Metals for Oxygen Reduction Reactions. *Phys. Chem. Chem. Phys.* **2011**, *13*, 15639−15643.
(50) Grimme, S. Semiempirical Gga-Type Density Functional Constructed with a Long-Range Dispersion Correction. *J. Comput. Chem.* **2006**, *27*, 1787−1799.
(51) Rossmeisl, J.; Logadottir, A.; Nørskov, J. K. Electrolysis of Water on (Oxidized) Metal Surfaces. *Chem. Phys.* **2005**, *319*, 178−184.
(52) Tripkovic, V.; Skulason, E.; Siahrostami, S.; Nørskov, J. K.; Rossmeisl, J. The Oxygen Reduction Reaction Mechanism on Pt(111) from Density Functional Theory Calculations. *Electrochim. Acta* **2010**, *55*, 7975−7981.
(53) Janik, M. J.; Taylor, C. D.; Neurock, M. First-Principles Analysis of the Initial Electroreduction Steps of Oxygen over Pt(111). *J. Electrochem. Soc.* **2009**, *156*, B126−B135.
(54) Sun, J.; Fan, Y.-H.; Liu, Z.-P. Electrocatalytic Oxygen Reduction Kinetics on Fe-Center of Nitrogen-Doped Graphene. *Phys. Chem. Chem. Phys.* **2014**, *16*, 13733−13740.
(55) Casalongue, H. S.; Ng, M. L.; Kaya, S.; Friebel, D.; Ogasawara, H.; Nilsson, A. In Situ Observation of Surface Species on Iridium Oxide Nanoparticles During the Oxygen Evolution Reaction. *Angew. Chem., Int. Ed.* **2014**, *53*, 1−5.
(56) Man, I. C.; Su, H. Y.; Calle-Vallejo, F.; Hansen, H. A.; Martinez, J. I.; Inoglu, N. G.; Kitchin, J.; Jaramillo, T. F.; Nørskov, J. K.; Rossmeisl, J. Universality in Oxygen Evolution Electrocatalysis on Oxide Surfaces. *ChemCatChem.* **2011**, *3*, 1159−1165.
(57) Nørskov, J. K.; Rossmeisl, J.; Logadottir, A.; Lindqvist, L.; Kitchin, J. R.; Bligaard, T.; Jonsson, H. Origin of the Overpotential for Oxygen Reduction at a Fuel-Cell Cathode. *J. Phys. Chem. B* **2004**, *108*, 17886−17892.
(58) Bajdich, M.; Garcia-Mota, M.; Vojvodic, A.; Nørskov, J. K.; Bell, A. T. Theoretical Investigation of the Activity of Cobalt Oxides for the Electrochemical Oxidation of Water. *J. Am. Chem. Soc.* **2013**, *135*, 13521−13530.
(59) Koper, M. T. M. Thermodynamic Theory of Multi-Electron Transfer Reactions: Implications for Electrocatalysis. *J. Electroanal. Chem.* **2011**, *660*, 254−260.

(60) Calle-Vallejo, F.; Inoglu, N. G.; Su, H. Y.; Martinez, J. I.; Man, I. C.; Koper, M. T. M.; Kitchin, J. R.; Rossmeisl, J. Number of Outer Electrons as Descriptor for Adsorption Processes on Transition Metals and Their Oxides. *Chem. Sci.* **2013**, *4*, 1245−1249.
(61) Mom, R. V.; Cheng, J.; Koper, M. T. M.; Sprik, M. Modeling the Oxygen Evolution Reaction on Metal Oxides: The Infuence of Unrestricted DFT Calculations. *J. Phys. Chem. C* **2014**, *118*, 4095−4102.
(62) CRC *Handbook of Chemistry and Physics*, 95th ed, 2014−2015. http://hbcponline.com/ (Accessed June 28, 2014).
(63) De Groot, M. T.; Koper, M. T. M. Redox Transitions of Chromium, Manganese, Iron, Cobalt and Nickel Protoporphyrins in Aqueous Solution. *Phys. Chem. Chem. Phys.* **2008**, *10*, 1023−1031.
(64) Baran, J. D.; Gronbeck, H.; Hellman, A. Analysis of Porphyrines as Catalysts for Electrochemical Reduction of O_2 and Oxidation of H_2O. *J. Am. Chem. Soc.* **2014**, *136*, 1320−1326.
(65) O'Halloran, K. P.; et al. Revisiting the Polyoxometalate-Based Late-Transition-Metal-Oxo Complexes: The "Oxo Wall" Stands. *Inorg. Chem.* **2012**, *51*, 7025−7031.
(66) Poverenov, E.; Efremenko, I.; Frenkel, A. I.; Ben-David, Y.; Shimon, L. J. W.; Leitus, G.; Konstantinovski, L.; Martin, J. M. L.; Milstein, D. Evidence for a Terminal Pt(IV)-Oxo Complex Exhibiting Diverse Reactivity. *Nature* **2008**, *455*, 1093−1096.
(67) Nam, W. High-Valent Iron(IV)-Oxo Complexes of Heme and Non-Heme Ligands in Oxygenation Reactions. *Acc. Chem. Res.* **2007**, *40*, 522−531.
(68) Gross, Z.; Nimri, S. A Pronounced Axial Ligand Effect on the Reactivity of Oxoiron(IV) Porphyrin Cation Radicals. *Inorg. Chem.* **1994**, *33*, 1731−1732.
(69) Liu, W.; Huang, X. Y.; Cheng, M. J.; Nielsen, R. J.; Goddard, W. A.; Groves, J. T. Oxidative Aliphatic C-H Fluorination with Fluoride Ion Catalyzed by a Manganese Porphyrin. *Science* **2012**, *337*, 1322−1325.
(70) Nappa, M. J.; Mckinney, R. J. Selectivity Control by Axial Ligand Modification in Manganese Porphyrin Catalyzed Oxidations. *Inorg. Chem.* **1988**, *27*, 3740−3745.
(71) Stephenson, N. A.; Bell, A. T. Mechanistic Insights into Iron Porphyrin-Catalyzed Olefin Epoxidation by Hydrogen Peroxide: Factors Controlling Activity and Selectivity. *J. Mol. Catal. A: Chem.* **2007**, *275*, 54−62.
(72) Olguin, J.; Muller-Bunz, H.; Albrecht, M. Springloaded Porphyrin NHC Hybrid Rhodium(III) Complexes: Carbene Dissociation and Oxidation Catalysis. *Chem. Commun.* **2014**, *50*, 3488−3490.
(73) Albrecht, M.; Maji, P.; Hausl, C.; Monney, A.; Muller-Bunz, H. N-Heterocyclic Carbene Bonding to Cobalt Porphyrin Complexes. *Inorg. Chim. Acta* **2012**, *380*, 90−95.
(74) Huang, J. S.; Yu, G. A.; Xie, J.; Wong, K. M.; Zhu, N. Y.; Che, C. M. Primary and Secondary Phosphine Complexes of Iron Porphyrins and Ruthenium Phthalocyanine: Synthesis, Structure, and P-H Bond Functionalization. *Inorg. Chem.* **2008**, *47*, 9166−9181.
(75) Simonneaux, G. Phosphines as Structural and Functional Probes of Hemoproteins. *Coord. Chem. Rev.* **1997**, *165*, 447−474.
(76) Sodano, P.; Simonneaux, G.; Toupet, L. Tertiary Phosphine Complexes of Iron Porphyrins - Synthesis, Molecular Stereochemistry, and Crystal-Structure of Bis(Dimethylphenylphosphine)-(Meso-5,10,15,20-Tetraphenylporphyrinato)Iron(II). *J. Chem. Soc., Dalton Trans.* **1988**, 2615−2620.
(77) Viswanathan, V.; Hansen, H. A.; Rossmeisl, J.; Nørskov, J. K. Universality in Oxygen Reduction Electrocatalysis on Metal Surfaces. *ACS Catal.* **2012**, *2*, 1654−1660.
(78) Shi, C. N.; Anson, F. C. Catalytic Pathways for the Electroreduction of Oxygen by Iron Tetrakis(4-N-Methylpyridyl)-Porphyrin or Iron Tetraphenylporphyrin Adsorbed on Edge Plane Pyrolytic-Graphite Electrodes. *Inorg. Chem.* **1990**, *29*, 4298−4305.
(79) Kalra, A.; Garde, S.; Hummer, G. Osmotic Water Transport through Carbon Nanotube Membranes. *Proc. Natl. Acad. Sci. U.S.A.* **2003**, *100*, 10175−10180.
(80) Hummer, G.; Rasaiah, J. C.; Noworyta, J. P. Water Conduction through the Hydrophobic Channel of a Carbon Nanotube. *Nature* **2001**, *414*, 188−190.
(81) Holt, J. K.; Park, H. G.; Wang, Y. M.; Stadermann, M.; Artyukhin, A. B.; Grigoropoulos, C. P.; Noy, A.; Bakajin, O. Fast Mass Transport through Sub-2-Nanometer Carbon Nanotubes. *Science* **2006**, *312*, 1034−1037.
(82) Skoulidas, A. I.; Ackerman, D. M.; Johnson, J. K.; Sholl, D. S. Rapid Transport of Gases in Carbon Nanotubes. *Phys. Rev. Lett.* **2002**, *89*.
(83) Dellago, C.; Naor, M. M.; Hummer, G. Proton Transport through Water-Filled Carbon Nanotubes. *Phys. Rev. Lett.* **2003**, *90*, 105902.
(84) Chen, J.; Li, X. Z.; Zhang, Q. F.; Michaelides, A.; Wang, E. G. Nature of Proton Transport in a Water-Filled Carbon Nanotube and in Liquid Water. *Phys. Chem. Chem. Phys.* **2013**, *15*, 6344−6349.
(85) Pang, P.; He, J.; Park, J. H.; Krstic, P. S.; Lindsay, S. Origin of Giant Ionic Currents in Carbon Nanotube Channels. *ACS Nano* **2011**, *5*, 7277−7283.
(86) Choi, W.; Ulissi, Z. W.; Shimizu, S. F. E.; Bellisario, D. O.; Ellison, M. D.; Strano, M. S. Diameter-Dependent Ion Transport through the Interior of Isolated Single-Walled Carbon Nanotubes. *Nat. Commun.* **2013**, *4*.
(87) Pfaff, F. F.; et al. An Oxocobalt(IV) Complex Stabilized by Lewis Acid Interactions with Scandium(III) Ions. *Angew. Chem., Int. Ed.* **2011**, *50*, 1711−1715.
(88) Hong, S.; Pfaff, F. F.; Kwon, E.; Wang, Y.; Seo, M.-S.; Bill, E.; Ray, K.; Nam, W. Spectroscopic Capture and Reactivity of a Low-Spin Cobalt(IV)-Oxo Complex Stabilized by Binding Redox-Inactive Metal Ions. *Angew. Chem., Int. Ed.* **2014**, *53*, 10403−10407.